

Sustainable Nanofibril Interfaces for Strain-Resilient and Multimodal Porous Bioelectronics

Ganggang Zhao, Zehua Chen, Shaoyun Wang, Sicheng Chen, Feng Zhang,
Syed Muntazir Andrabi, Yadong Xu, Qunle Ouyang, Milton Eric Busquets Rosas,
Xiaoyan Qian, Jingwei Xie, and Zheng Yan*

Porous soft bioelectronics have attracted significant attention due to their high breathability, long-term biocompatibility, and other unique features inaccessible in nonporous counterparts. However, fabricating high-quality multimodal bioelectronic components that operate stably under strain on porous substrates, along with integrating microfluidics for sweat management, remains challenging. In this study, cellulose nanofibrils (CNF) are explored, biomass-derived sustainable biomaterials, as nanofibril interfaces with unprecedented interfacial robustness to enable high-quality printing of strain-resilient bioelectronics on porous substrates by reducing surface roughness and creating mechanical heterogeneity. Also, CNF-based microfluidics can provide continuous sweat collection and refreshment, crucial for accurate biochemical sensing. Building upon these advancements, a multimodal porous wearable bioelectronic system is further developed capable of simultaneously detecting electrocardiograms and glucose and beta-hydroxybutyrate in sweat for monitoring energy metabolism and consumption. This work introduces novel strategies for fabricating high-quality, strain-resilient porous bioelectronics with customizable multimodalities to meet arising personalized healthcare needs.

1. Introduction

Next-generation soft bioelectronics should facilitate long-term, high-fidelity monitoring of multiple, vital biophysical and biochemical signals throughout daily activities.^[1-3] In this context, porous soft bioelectronics have recently garnered significant interest owing to their high breathability, which can effectively minimize sweat accumulation-caused inflammation and performance degradation, benefiting their long-term on-body operation.^[4-6] Additionally, porous devices can incorporate features such as self-cooling^[7-9] and antimicrobial properties^[4,10,11] through structural design and the integration of functional molecules. Typically, porous bioelectronic devices consist of customized bioelectronic components patterned on porous soft substrates. These substrates mainly include textiles and various porous soft materials made by electrospinning, phase

G. Zhao, S. Wang, Q. Ouyang, Z. Yan
Department of Mechanical & Aerospace Engineering
University of Missouri
Columbia, MO 65201, USA
E-mail: yanzheng@missouri.edu

Z. Chen, S. Chen, F. Zhang, X. Qian, Z. Yan
Department of Chemical and Biomedical Engineering
University of Missouri
Columbia, MO 65201, USA

S. M. Andrabi, M. E. B. Rosas, J. Xie
Department of Surgery-Transplant and Mary and Dick Holland
Regenerative Medicine Program
University of Nebraska Medical Center
Omaha, NE 68198, USA

Y. Xu
Andrew and Peggy Cherng Department of Medical Engineering
Division of Engineering and Applied Science
California Institute of Technology
Pasadena, CA 91125, USA

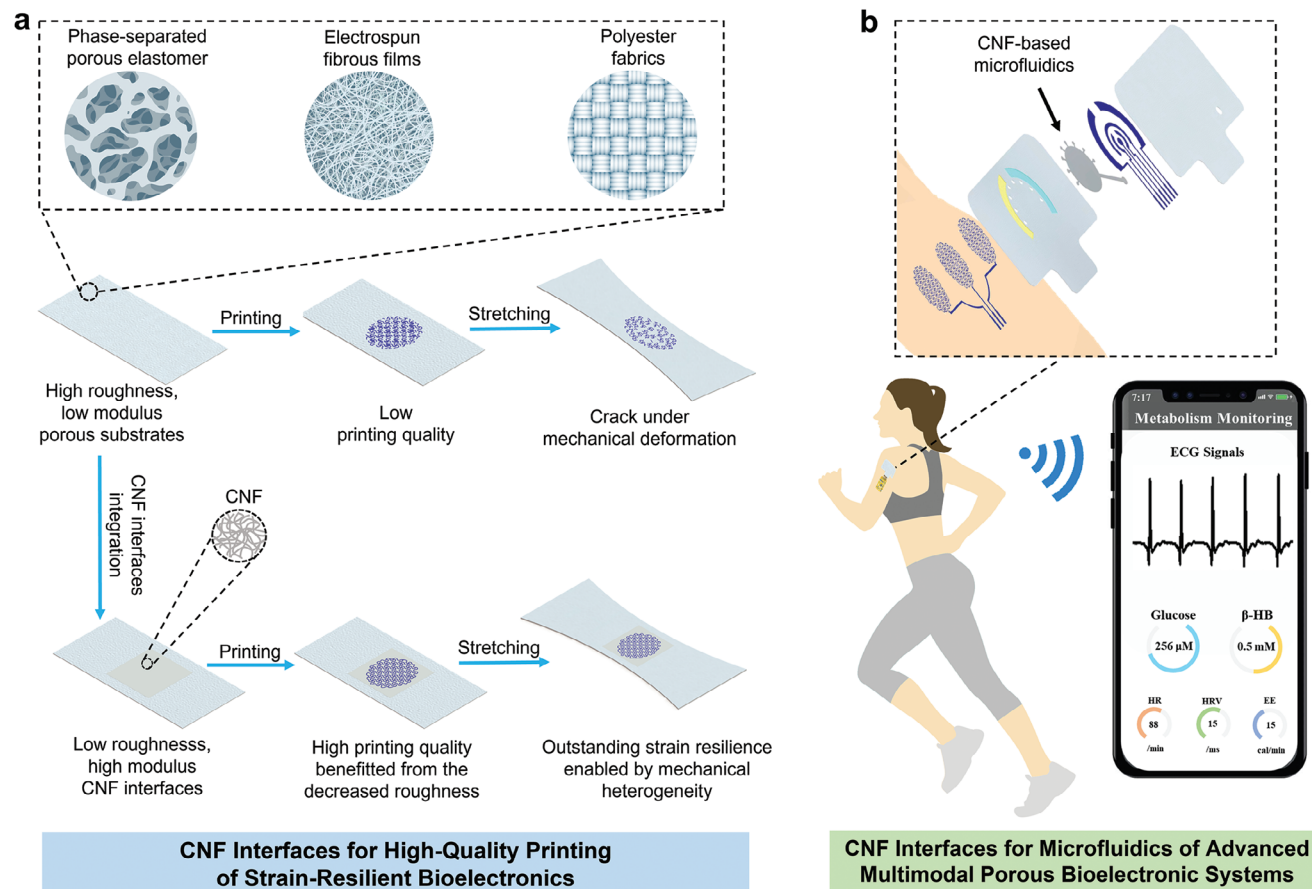
Z. Yan
NextGen Precision Health
University of Missouri
Columbia, MO 65211, USA

 The ORCID identification number(s) for the author(s) of this article
can be found under <https://doi.org/10.1002/adma.202411587>

DOI: [10.1002/adma.202411587](https://doi.org/10.1002/adma.202411587)

separation, and others.^[10,12-15] Bioelectronic device fabrication on these substrates can be achieved with lithograph-based techniques, mask-involved fabrication, and laser-assisted manufacturing.^[4,5,16-18] Compared to these fabrication techniques, mask-free additive manufacturing (such as inkjet printing and extrusion printing) provides a promising avenue for the scalable and easily customizable manufacturing of biophysical and biochemical sensors and other bioelectronic components through appropriate ink formulations.^[19-21] However, it remains a challenge to produce high-quality bioelectronic components with solution printing on porous substrates, largely because of their inherent surface roughness. Furthermore, ensuring that bioelectronic components are strain-resistant to maintain stable function under strain, together with integrating judiciously designed microfluidic systems for accurate biochemical analysis, presents further challenges to the development of advanced porous soft bioelectronic systems with customized multimodalities.

Cellulose, Earth's most abundant and sustainable biopolymer, is characterized by its structured fibrous arrays with specific orientations.^[22-24] Through various top-down methodologies, cellulose can be deconstructed into fibrils and further refined into cellulose nanofibrils (CNF).^[25] CNF exhibits



CNF Interfaces for High-Quality Printing of Strain-Resilient Bioelectronics

CNF Interfaces for Microfluidics of Advanced Multimodal Porous Bioelectronic Systems

Figure 1. Conceptual illustration of CNF interfaces to enable high-quality printing and stain resilience (a) and microfluidics (b) in porous soft bioelectronics. This study proposes a strategy to integrate CNF interfaces on porous substrates (such as phase-separated porous elastomers, electrospun porous films, and polyester fabrics) for fabricating multimodal porous soft bioelectronics (a). CNF integration smooths the surface roughness of porous substrates to facilitate high-quality bioelectronics printing while tailoring surface stiffness and creating mechanical heterogeneity to offer outstanding strain resilience. Additionally, guided by theoretical simulations, CNF-based microfluidics have been developed for sweat management and precise biochemical sensing. Building on these advancements, we have developed an exemplary device capable of simultaneously detecting ECG, sweat glucose, and β -HB for monitoring energy metabolism and consumption (b). The collected data can be processed *in situ* and wirelessly transmitted for graphical display on smartphones via flexible printed circuit boards.

remarkable mechanical properties (elastic modulus: ≈ 1 GPa),^[22] allowing for stiffness tailoring and strain regulation when interfaced with soft materials. Additionally, chemical modification enables CNF to form strong bonds with other substances through their intrinsic hydroxyl groups.^[26–28] Besides, solution-casted CNF typically possess mesoporous structures with high flatness^[29] that can improve ink absorption^[30,31] and enhance printing quality, thus making them ideal for high-quality bioelectronics printing. Moreover, the intrinsic hydrophilicity and tailorability of formed porous structures render CNF well-suited for building microfluidic channels. Also, the use of sustainable materials like CNF ensures a renewable and eco-friendly approach to developing advanced bioelectronics. Despite these attributes, exploring sustainable CNF interfaces for soft bioelectronics applications is still rare.

This work explores sustainable CNF interfaces and their applications in enabling high-quality printing, strain resilience, and microfluidics in porous soft bioelectronics. As illustrated in Figure 1, CNF can be patterned onto a variety of commonly used

porous substrates for surface flatness and stiffness tailoring, critical for the high-quality printing of bioelectronic components with outstanding strain resilience. Also, robust interfacial bonding is achieved between CNF and porous substrates because of the CNF's partial infiltration into the porous matrix to increase contact areas and the formation of hydrogen bonds, as verified by our experimental studies and molecular dynamics (MD) simulations. Besides, our experimental results and finite element analysis (FEA) simulations indicate that judiciously tailored CNF patterns on porous substrates can function as microfluidic channels, enabling continuous sweat collection and refreshing, essential for accurate biochemical sensing. Composites of poly(3,4-ethylenedioxythiophene) (styrene sulfonate) (PEDOT: PSS) and silver nanowires (AgNWs) are formulated as universal inks for printing various bioelectronic components on CNF-interfaced porous substrates. Based on these advancements, we have developed a multimodal porous wearable bioelectronic system capable of concurrently monitoring glucose and beta-hydroxybutyrate (β -HB) levels in sweat and electrocardiograms (ECG), providing

insights into energy metabolism and consumption. Key related physiological signals, including heart rate (HR), heart rate variability (HRV), and energy expenditure (EE), can be derived from ECG. The collected data is in situ processed and wirelessly transmitted for graphical display on smartphones via flexible printed circuit boards.

2. Results

2.1. CNF Integration and Bioelectronics Printing on Porous Substrates

In this work, we investigate CNF integration and bioelectronics printing mainly using phase-separated, multifunctional porous styrene-ethylene-butylene-styrene (SEBS) as the model substrate example (Figure S1, Supporting Information). We explore the CNF integration using extrusion printing and study the effects of CNF lengths on ink formulations. Here, commercially sourced softwood pulp is treated with 2,2,6,6-tetramethylpiperidine-1-oxyl to oxidize cellulose C6 hydroxyl groups into carboxyl groups, thus promoting the disintegration of elementary fibrils and facilitating the isolation of microfibrils. Following ultrasonication, a homogeneous CNF dispersion is obtained, with the CNF lengths and widths controlled by adjusting ultrasonication amplitudes. In this work, two types of CNF, L-CNF (diameter: ≈ 15 nm; length: ≈ 2 μm) and S-CNF (diameter: ≈ 6 nm; length: ≈ 400 nm), are prepared for ink formulations (Figure 2a; Figure S2, Supporting Information). To develop suitable ink formulations, we investigate the rheological behavior of the S-CNF inks at varying weight concentrations. Increasing the S-CNF ink concentration from 1% to 3% raises the viscosity from 0.1 to 10 Pa·s at a shear rate of 1 s^{-1} (Figure S3a, Supporting Information), suboptimal for extrusion printing. Additionally, the viscoelastic characteristics of the S-CNF inks (Figure S3b, Supporting Information) show yield stress below 10 Pa, causing lateral spreading during extrusion printing. Further increasing the concentration results in ink homogeneity. To address this issue, we incorporate L-CNF in the ink formulations. Rheological evaluations (Figure S4, Supporting Information) indicate that the L-CNF ink possesses lower viscosity and yield stress compared to S-CNF inks at the same concentrations. Our investigations further reveal that ink formulations comprising a blend of S-CNF and L-CNF exhibit superior viscosity and yield stress (Figure 2b; Figure S5, Supporting Information) compared to the inks composed solely of L-CNF at equivalent concentrations. The mixture forms a better network of fibril interactions, thus enhancing printability and bonding forces to porous SEBS (Figure S6, Supporting Information). Adopting a balanced approach, we have selected a mixed ink formulation containing 2% S-CNF and 2% L-CNF for subsequent CNF printing to harmonize printability with strong interfacial bonding. As shown in Figure 2c-f, CNF integration significantly reduces the surface roughness of porous SEBS from ≈ 6.79 μm to 0.18 μm . Although the integration of CNF interfaces reduces the water vapor transmission rate (WVTR) of porous SEBS, it remains significantly higher than the static human sweat rate (≈ 25 g m^{-2} h^{-1}),^[6] the WVTR of human skin (8.5 g m^{-2} h^{-1}),^[32] and that of nonporous SEBS (3.0 g m^{-2} h^{-1}),^[7] while retaining long-term stability (Figure S7, Supporting Information). This ensures that CNF-interfaced porous SEBS maintains adequate breathability

for effective sweat vapor transmission. During intense exercise, when sweat production may exceed the device's WVTR, the integrated microfluidic channels can effectively discharge excess liquid sweat. Figure 2h and Figure S8 (Supporting Information) show various CNF patterns printed onto porous SEBS using extrusion printing, highlighting the versatility and precision of integrating CNF patterns with arbitrary shapes on porous elastomer substrates.

We further investigate the solution printing of PEDOT: PSS and AgNWs on CNF-interfaced porous SEBS because of their synergistic effects, which can serve as the universal inks for building various bioelectronic components (such as conductive paths, antennas, biochemical sensors, and biophysical sensors).^[33,34] As depicted in Figures S9 and S10 (Supporting Information) AgNWs can provide high electrical conductivity, while PEDOT: PSS can enhance long-term stability and offer outstanding electrochemical activity. We have examined extrusion printing and inkjet printing of PEDOT: PSS and AgNWs, two widely used printing techniques. For extrusion printing, composite inks of PEDOT: PSS and AgNWs are formulated (Figure 2i; Figure S11, Supporting Information). In the case of inkjet printing, individual inks of PEDOT: PSS and AgNWs are prepared for layer-by-layer printing to create composites (Figure S12, Supporting Information). As shown in Figure 2j and Figure S13 (Supporting Information), the uncontrolled capillary forces arising from the nonuniform distribution of micrometer-sized pores in porous SEBS can cause inks to spread randomly, leading to the deformation of printed patterns. The integration of CNF interfaces can address this issue owing to their narrow-distributed nanoporous structures (<100 nm; Figure 2e) and reduced surface roughness (Figure 2f). Figure 2k,l and Figure S14 (Supporting Information) demonstrate that high-quality patterning of conductive lines with various widths can be achieved on CNF-interfaced porous SEBS using both inkjet printing and extrusion printing. For instance, the lines printed on CNF-interfaced porous SEBS exhibit sharp edges, whereas the lines printed directly on porous SEBS show noticeable imperfections. The efficacy of CNF interfaces is further corroborated by current-voltage curves in Figure 2l and Figure S14 (Supporting Information) showing a dramatic reduction in resistance by a factor of $\approx 10\ 000\ 000$ for 30 μm wide lines printed on CNF-interfaced porous SEBS compared to those printed on bare porous SEBS. Furthermore, complex patterns and arrays of PEDOT: PSS and AgNWs with various sizes can be achieved on CNF-interfaced porous SEBS, as illustrated in Figure 2m (inkjet printed), Figure 2n (extrusion printed) and Figure S15 (Supporting Information, extrusion printed), indicating the potential for printing advanced bioelectronic components with various customized functions. The cross-sectional scanning electron microscope (SEM) image in Figure 2o illustrates the interface of the composite ink of PEDOT: PSS and AgNWs, CNF interfaces, and porous SEBS.

2.2. CNF Interfaces for Strain-Resilient Porous Soft Bioelectronics

In addition to facilitating high-quality bioelectronics printing, CNF interfaces can also endow printed bioelectronics with outstanding strain resilience due to their stiffness heterogeneity

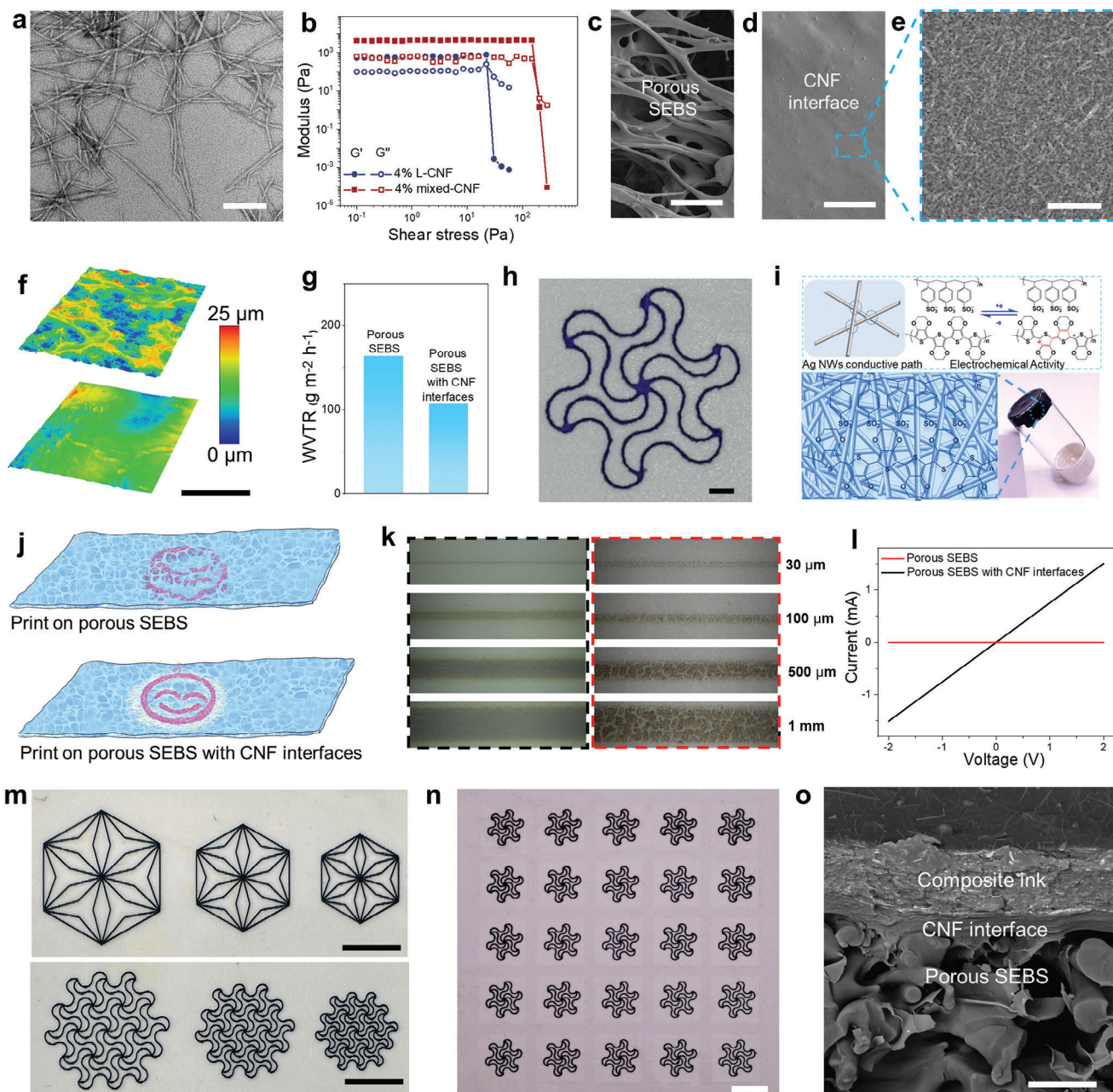


Figure 2. CNF integration and bioelectronics printing on porous substrates. a) TEM image of S-CNF. Scale bar: 100 nm. b) The storage modulus, G' , and loss modulus, G'' , as a function of shear stress for 4% L-CNF inks and mixed inks (2% L-CNF and 2% S-CNF). SEM images of porous SEBS (c) and CNF interfaces on porous SEBS (d, e). Scale bars: 20 μm in (c, d) and 500 nm in (e). f) 3D laser scanning microscope image of porous SEBS without (top) and with CNF interfaces (bottom), indicating surface flattening (from ≈ 6.79 to $0.18 \mu\text{m}$ in surface roughness) due to CNF integration. The color bar indicates the height distribution of the scanned surfaces. Scale bar: 300 μm . g) Water vapor transmission rates (WVTR) of porous SEBS without (left) and with (right) CNF interfaces, demonstrating CNF integration has minimal influence on the breathability of porous SEBS. h) Optical image of the serpentine pattern of CNF (stained by violet dye) printed onto porous SEBS. Scale bar: 2 mm. i) Schematic illustration of the PEDOT:PSS/AgNWs composite ink used for extrusion printing. The inset is an optical image of the composite ink. j) Conceptual illustration of CNF integration on porous SEBS contributing to high-quality printing. The corresponding optical images are provided in Figure S13, Supporting Information. k) Optical images of inkjet-printed conductive lines with various widths on porous SEBS with (left) and without (right) CNF interfaces. l) Current-voltage curves of inkjet-printed conductive lines (30 μm in width) on porous SEBS with (black) and without (red) CNF interfaces. m, n) Various conductive patterns printed using inkjet printing (m) and extrusion printing (n) on porous SEBS with CNF interfaces. o) Cross-sectional SEM image of the composite ink of PEDOT:PSS/AgNWs printed on porous SEBS with CNF interfaces. Scale bars: 2.5 mm in (m), 1 cm in (n), and 10 μm in (o).

and robust interfacial bonding with porous elastomer substrates (**Figure 3a**). FEA simulations (left panel, **Figure 3b**) and experimental validations from digital image correlation (DIC) techniques (right panel, **Figure 3b**) show that the strain on the serpentine-swirl pattern of CNF is less than 1% when the sample is bi-axially stretched to 100%, showing outstanding strain-isolation effects. **Figure S16** (Supporting Information) further corroborates these effects for the CNF square pattern printed on porous SEBS, underscoring the versatility of CNF interfaces in strain isolation. Additionally, SEM images (**Figure S17**, Supporting Information) show that PEDOT: PSS/AgNWs printed on CNF interfaces retain excellent structural integrity, further highlighting the exceptional strain resilience and strain isolation performance of the CNF interfaces. A key challenge in soft bioelectronics is the weak interface when integrating soft materials with relatively rigid functional components.^[35] CNF printed on porous SEBS demonstrate robust interfaces, as illustrated in Figures **S18–S20** (Supporting Information) and **Figure 3c–e**. Here, the porous structure of SEBS enhances the system's strain resistance in two ways. First, the porous structure reduces the elastic modulus of the SEBS substrate compared to nonporous SEBS,^[7] allowing strain-induced stress to primarily deform the low-modulus SEBS substrate while preserving the stability of stiff CNF interfaces and reducing stress concentration at the edges of the CNF patterns (**Figure S18**, Supporting Information). Second, the porous structure facilitates deeper penetration of the CNF ink into the SEBS layers, increasing the contact area and forming a robust CNF-SEBS interface (**Figure 3e**). This strong interface is essential for maintaining the mechanical integrity of the device and further improving its strain resistance. MD simulations provide quantitative evidence of robust interfacial bonds, with **Figure 3c** and **Figure S19** (Supporting Information) showing abundant hydrogen bonds at the interfaces between CNF and porous SEBS. In contrast, almost no hydrogen bonds are observed at the interface between CNF and nonporous SEBS due to contact distances exceeding the hydrogen bond length (2.8 Å), as depicted in **Figure S20**, Supporting Information. Further experimental evidence of strong interfacial bonding is presented by peeling test results in **Figure S6** (Supporting Information), recording an interfacial adhesive strength of ≈380 N m⁻¹, sufficient to support a weight of 500 grams (**Figure 3d**). The cross-section SEM image in **Figure 3e** reveals the penetration of CNF into the porous substrate, increasing the contact area and forming a robust interface crucial for mechanical integrity and robustness. These results demonstrate the exceptional resilience and stability of CNF interfaces on porous SEBS under stretching, which can maintain the performance of bioelectronic devices printed atop them under mechanical deformation, a highly desirable feature for soft bioelectronics.

We further demonstrate the efficacy of CNF interfaces in endowing strain resilience by using three representative bioelectronic components as model examples, including conductive paths for wireless powering systems, electrophysiological sensors, and biochemical sensors. **Figure 3f(i)** and **Figure S21** (Supporting Information) indicate that conductive paths printed on CNF interfaces on porous SEBS maintain stable electrical conductivity even under 100% uniaxial and biaxial stretching. In contrast, conductive paths printed on porous SEBS without CNF ex-

perience a dramatic electrical resistance increase (more than a 10 000 000-fold increase at 100% strain). Notably, optical images [insets, **Figure 3f(i)**] reveal no obvious deformation for the conductive path printed on CNF interfaces on porous SEBS (black dashed lines), whereas the conductive path printed on porous SEBS without CNF (black dashed lines) exhibits obvious fractures. Furthermore, the conductive path printed on CNF interfaces on porous SEBS shows a marginal resistance change of ≈2.5% even after 2000 stretching cycles at 50% strain (**Figure S22**, Supporting Information), indicating the high robustness and durability of CNF-porous SEBS interfaces. In addition, a near-field communication (NFC)-based wireless powering system of a light-emitting diode (LED) is developed using conductive paths to build the antenna [inset, **Figure 3f(ii)**]. Quantitative assessments of LED illuminance display the outstanding operational stability and reliability of the wireless powering system up to 100% strain when fabricated onto CNF interfaces on porous SEBS [black curve, **Figure 3f(ii)** and **Figure S23**, Supporting Information]. Conversely, the LED powered through the antenna fabricated on porous SEBS without CNF exhibits rapid degradation and electrical failure under a mere 20% strain [red curve, **Figure 3f(ii)**]. Furthermore, the stable electrode-skin contact impedance is crucial for high-fidelity recordings of electrophysiological signals during human motion.³ The electrode-skin contact impedance for the electrode printed onto CNF interfaces on porous SEBS remains almost unchanged (≈1% change at 100 Hz) under 100% strain [**Figure 3g(i)**], while a significant increase in the contact impedance (over 500% change at 100 Hz) is observed for the electrode printed on porous SEBS without CNF (**Figure S24**, Supporting Information). ECG biosignals recorded with the electrodes on CNF interfaces display negligible signal deterioration, with a signal-to-noise ratio (SNR) of 28.7 dB before strain and 28.4 dB at 100% strain [top panel, **Figure 3g(ii)**]. In contrast, ECG signals captured with electrodes on porous SEBS without CNF exhibit a comparable SNR of 28.5 dB without strain but become indiscernible at 100% strain [bottom panel, **Figure 3g(ii)**]. Sweat biochemical sensors can offer valuable insights into human health at the molecular level, and their stable operation under deformation is crucial for effective health monitoring.^[36–38] Cyclic voltammogram curves [**Figure 3h(i)**] and electrochemical impedance spectroscopy (EIS) analyses (**Figure S25**, Supporting Information) demonstrate that electrodes of PEDOT: PSS and AgNWs composites printed on CNF interfaces on porous SEBS maintain stable electrochemical performance even under 100% stretching. In contrast, electrodes printed on porous SEBS without CNF show degraded functionality under the same strain condition **Figure S26**, Supporting Information. We have further fabricated bioelectronic sensors for sodium ion (Na⁺) measurements based on open-circuit potentials [**Figure 3h(ii)**] and **Figure S27**, Supporting Information] and glucose and β-HB detections based on chronoamperometry (Figures **S28** and **S29**, Supporting Information). These biosensors display high selectivity and sensitivity and stable performance (with <1% sensitivity change) even under 100% strain. The 7-day period tests show the long-term stability of biochemical sensing (Figures **S28e** and **S29e**, Supporting Information). Additionally, the stability of the bioelectronic device was further validated by its consistent performance during 100 cycles of rubbing (**Figure S30**, Supporting Information).

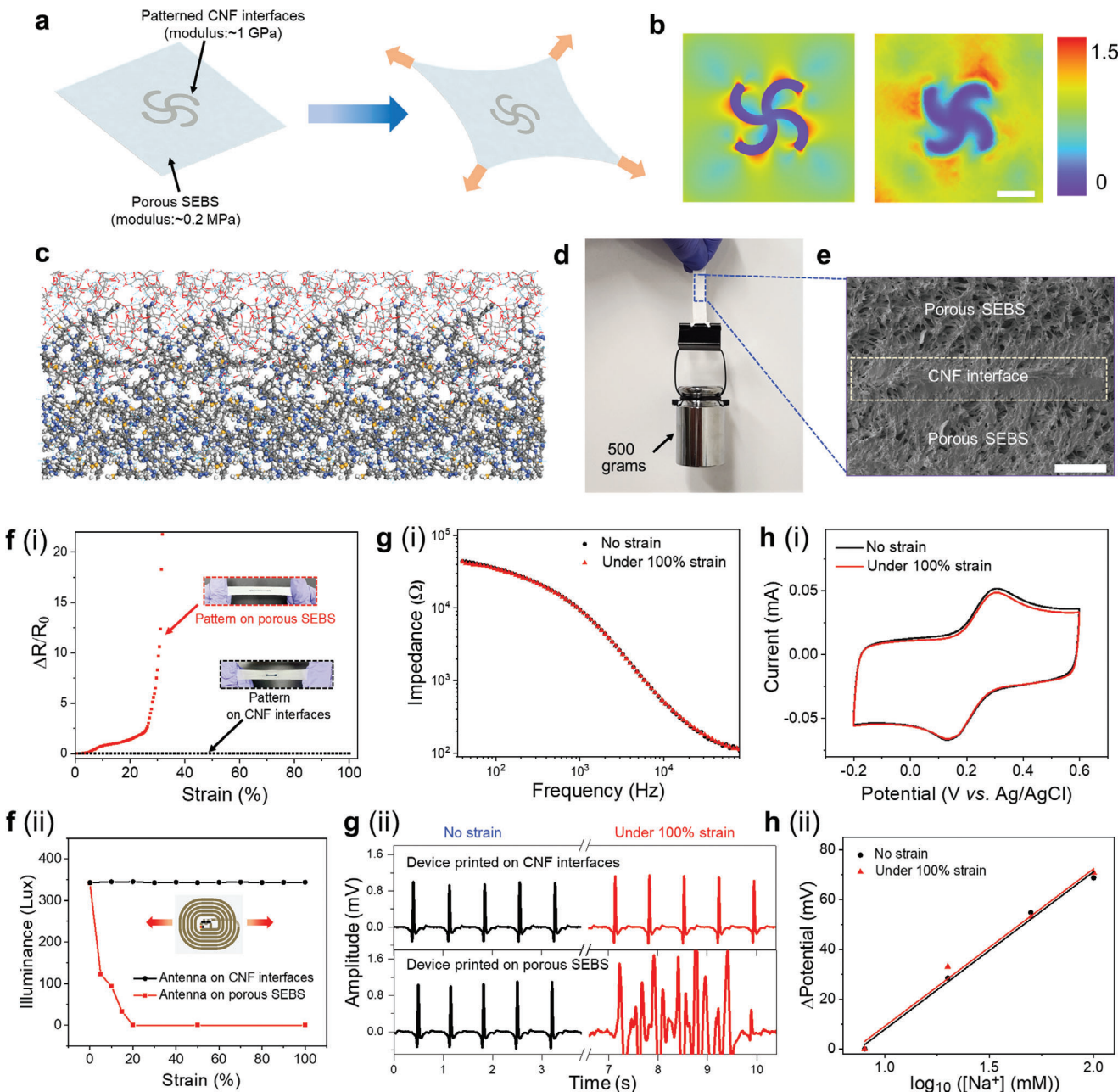


Figure 3. CNF interfaces for strain-resilient porous soft bioelectronics. a) Schematic illustration of strain resilience of the serpentine-swirl pattern of CNF on porous SEBS owing to their mechanical heterogeneity and robust interfacial bonding. b) FEA simulations of the strain-isolation effect of the serpentine-swirl pattern of CNF printed on porous SEBS (left) under 100% biaxial stretching and the corresponding experimental results (right). The color bar indicates the strain distribution. Scale bar: 1 cm. c) MD simulations of interfacial bonding between CNF and porous SEBS. Hydrogen bonds are highlighted in red. d) Optical image of the robust interfacial bonding between CNF and porous SEBS, which is strong enough to support a weight of 500 grams. e) Cross-sectional SEM image, highlighting the interfaces of the sandwich structure consisting of the porous SEBS, CNF, and porous SEBS. Scale bar: 100 μ m. f) i) Relative resistance changes ($\Delta R/R_0$) of the printed conductive patterns on porous SEBS without (red) and with CNF interfaces (black) as a function of the uniaxial strain. The insets are corresponding optical images of conductive patterns under 100% uniaxial stretching. ii) Quantitative illuminance analysis of LED wirelessly powered by the antennas printed on porous SEBS without (red) and with CNF interfaces (black). The inset shows the wireless LED powering system under axial stretching. g) i) Device-skin contact impedances of electrophysiological electrodes printed on porous SEBS with CNF interfaces: no strain (black) and 100% strain (red). ii) ECG signals recorded using electrophysiological electrodes printed on porous SEBS with (top) and without CNF interfaces (bottom): no strain (black) and under 100% strain (red). The ECG signals are captured from the chest skin of a human subject. h) i) Cyclic voltammogram curves of electrochemical biosensing electrodes printed on porous SEBS with CNF interfaces tested in the 0.1 M KCl solution with 10 mM $[Fe(CN)_6]^{3-/4-}$ under the scan rate of 10 $mv\ s^{-1}$: no strain (black) and 100% strain (red). ii) Calibration linear plots of the Na^+ biosensor printed on porous SEBS with CNF interfaces: no strain (black) and under 100% strain (red).

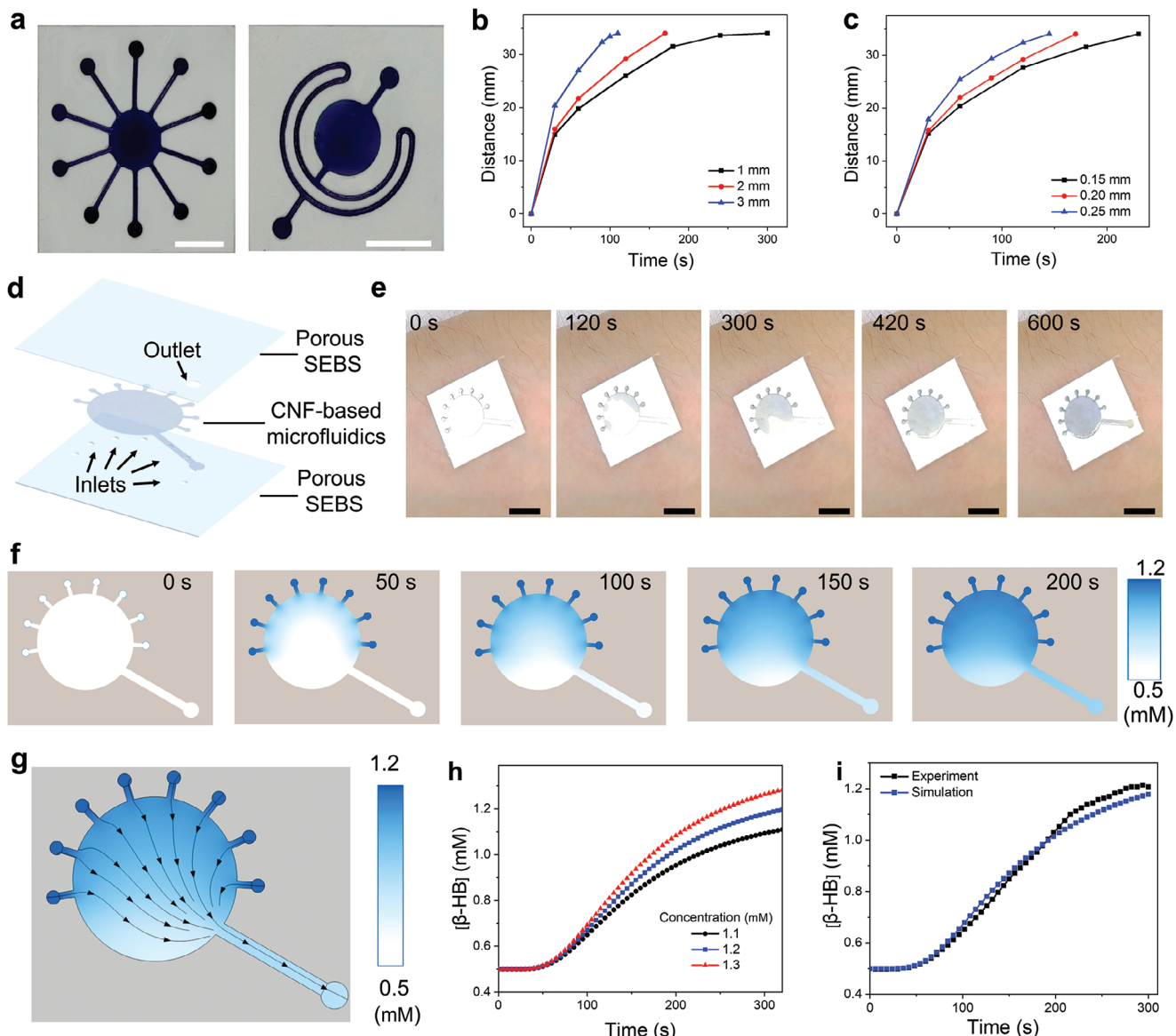


Figure 4. CNF-based microfluidics for porous soft bioelectronics. a) Optical images of CNF-based microfluidic channels on porous SEBS, wetted by stained water. Scale bars: 5 mm. Relationships between the liquid travel time and travel distance in CNF-based microfluidic channels with varying channel widths (b) and channel thicknesses (c). d) Schematic illustration of the wearable microfluidic system used for characterization, which can serve as the basis to construct the microfluidic system for wearable sweat biochemical sensors. e) Optical images of sweat filling the CNF-based microfluidic channels during the iontophoresis-induced sweat sampling. Agarose hydrogels loaded with carbachol on anodes and KCl on cathodes are employed for iontophoresis-enabled on-demand sweat extraction. Scale bars: 5 mm. f) FEA simulations of the microfluidic refreshing process of β -HB, showing a concentration change from 0.5 to 1.2 mM. g) Fluidic diagram from the FEA simulation at the 200 s during the β -HB refreshing process. h) Simulations of time evolution of concentration changes during refreshing using β -HB solutions of different concentrations. i) Time evolution of concentration changes obtained from FEA simulations and experimental results, indicating good agreement.

2.3. CNF-Based Microfluidics for Porous Soft Bioelectronics

The integration of microfluidics into wearable sweat sensors improves biochemical sensing accuracy by continuously delivering freshly secreted sweat to the sensor region. Traditional wearable microfluidic systems are typically made by patterning hollow microfluidic channels on flexible substrates, which are not suitable for porous bioelectronics.^[36,39] In this work, we have developed CNF-based wearable microfluidic systems on porous

substrates. By tailoring the fabrication process of CNF interfaces, we have increased porosity and enhanced wicking rates, thereby facilitating the efficient transport of extracted sweat. For example, Figure 4a demonstrates that dyed water efficiently disperses across CNF-based microfluidic channels without diffusing into the adjacent porous SEBS substrates. Before designing wearable microfluidic systems, we investigated the liquid-wicking kinetics of CNF-based channels by measuring the travel distance and corresponding time for channels of varying widths

and thicknesses. Figure 4b shows that for a constant channel thickness of 0.2 mm, the travel distance within the channel increases with the channel width over the same time. Similarly, Figure 4c illustrates that for a channel of constant width (2 mm), the travel distance increases with the channel thickness over a given time. Applying the simplified Washburn equation ($L = D\sqrt{t}$),^[40] where L is the travel distance, D is the diffusion coefficient depending on the channel size and liquid properties, and t is the travel time, we have calculated D values of channels with specific thickness of 0.2 mm: 2.18 mm s^{-1/2} for 1 mm width, 2.60 mm s^{-1/2} for 2 mm width, and 3.28 mm s^{-1/2} for 3 mm width. The travel speeds for channels with a fixed width of 2 mm are 2.24 mm s^{-1/2} for a 0.15 mm thickness and 2.87 mm s^{-1/2} for a 0.25 mm thickness. Details are provided in Note S1 (Supporting Information). Leveraging insights gained from liquid travel speed calculations, CNF-based microfluidics systems are judiciously designed to enhance sweat collection and refresh efficiency. As illustrated in Figure 4d, this microfluidic system features a thickness of 0.2 mm, with eight inlets converging into an outlet channel. The outlet channel is characterized by a length of 8.7 mm and a width of 1 mm. This configuration achieves a wicking rate of 13 μL min⁻¹, ensuring the timely collection and discharge of sweat, which is critical for maintaining the integrity of sweat analysis over extended periods of wear.

The on-body sweat sampling experiment (Figure 4e; Movie S1, Supporting Information) showcases the capability of CNF-based microfluidic systems for rapid sweat collection. Notably, the sensing chamber achieves complete filling in ≈7 min after sweat induction via iontophoresis, which agrees well with the FEA simulations Figure S31 (Supporting Information). To further explore the performance of CNF-based microfluidic systems, FEA is employed to examine the refresh time in response to changes in concentrations of β-HB and glucose (Movie S2, Supporting Information), which are the two biomarkers involved in wearable prototype device demonstration in Figure 5. The analysis focuses on the time required for the CNF-based microfluidic system to adjust to 90% of a new solution concentration following a change. For a concentration shift of β-HB from 0.5 to 1.2 mM, the refresh time is found to be ≈3.8 min, as depicted in Figure 4f. A streamline diagram of the CNF-based microfluidic system at 200 s (Figure 4g) shows the direction and state of sweat flow within the system. Additionally, when evaluating the refresh time for varying concentrations of β-HB specifically changes from 0.5 to 1.1 mM and from 0.5 to 1.3 mM, the system demonstrates refresh times of 3.6 min (for 1.1 mM) and 4 min (for 1.3 mM), respectively, as shown in Figure 4h. This indicates minimal variation in refresh time despite different concentration changes. Similar outcomes are observed for the glucose, as detailed in Figure S32 (Supporting Information). The experimental data for β-HB and glucose concentrations over time (Figure 4i; Figure S32c, Supporting Information) correlate closely with the simulation results, validating the ability of CNF-based microfluidic systems to rapidly refresh in response to changes in sweat compositions. To further enhance the reliability of the comparison between the experimental results and the simulation, a Chi-square goodness-of-fit test at the 95% confidence level was conducted. The results indicate that the experimental data fit well with the simulated values. These results underpin the potential of CNF-based microfluidics for real-time monitoring of sweat biomarkers.

2.4. Porous Wearable Soft Bioelectronics for Energy Metabolism and Consumption Monitoring

As depicted in Figure 5a and its caption, we have further developed an exemplary example of multimodal porous soft bioelectronics for customized healthcare applications. The device can provide on-demand sweat extraction and real-time detections of sweat glucose and β-HB levels for energy metabolism monitoring, as well as ECG recording for energy consumption management. From ECG signals, we can further determine HR, HRV, and EE.^[43–45] These sensors are fabricated on CNF-interfaced porous SEBS. Experimental characterizations display their high fidelity and outstanding strain resilience (Figure 3g(ii)) for ECG sensors, Figure S28 (Supporting Information) for glucose sensors, and Figure S29 (Supporting Information) for β-HB sensors). Agarose hydrogels loaded with carbachol on anodes and KCl on cathodes are employed for ionophoresis-enabled on-demand sweat extraction (Figure 4e), and CNF-based microfluidic systems (Figure 4d) are utilized for sweat collection and refreshing. The device demonstrates long-term structural stability, showing no signs of layer delamination during the 7-day on-skin test (Figures S33, Supporting Information). By integrating with flexible printed circuit boards (Figures S33, S34 and Table S1, Supporting Information), the device can achieve in situ data processing and wireless data transmission for graphic display on smartphones (Movie S3, Supporting Information).

As shown in Figure 5b,c, the device is employed to monitor energy metabolism and consumption from a human subject. The device is attached to the upper arm of the human subject for the signal recording (Note S2, Supporting Information). The upper arm, rich in sweat glands, is ideal for sweat biochemical sensing.^[46,47] Furthermore, recent studies indicate that the upper arm is a highly preferred body location for users to wear wearable devices.^[48,49] Additionally, ECG signals with sufficient qualities can be recorded from one single arm (Figure S35, Supporting Information). The 7-day period tests show the long-term stability of ECG recording (Figure S36, Supporting Information). We observe that the human volunteer, after fasting for 12 h, exhibited low glucose concentrations while relatively high β-HB levels in sweat. In the first scenario (Figure 5b), representing the typical ketone metabolism, the fasting volunteer consumed a keto drink, resulting in an increase in β-HB levels and a further decrease in glucose levels. This trend persisted until the intake of carbohydrates. In the second scenario (Figure 5c), under the carbohydrate metabolism, the fasting volunteer consumed bread, leading to a sharp decline in β-HB levels and an increase in glucose levels, with glucose levels gradually decreasing over time, while β-HB levels exhibited the opposite trend. The consumption of a keto drink further increased β-HB concentrations. In addition to biochemical monitoring, HR and HRV were successfully tracked, and the increase in HR and a decrease in HRV due to cycling were observed in both scenarios (Figure 5b,c). The energy expenditure (i.e., EE) calculated from the heart rate was also obtained. The ability of our porous device to monitor the

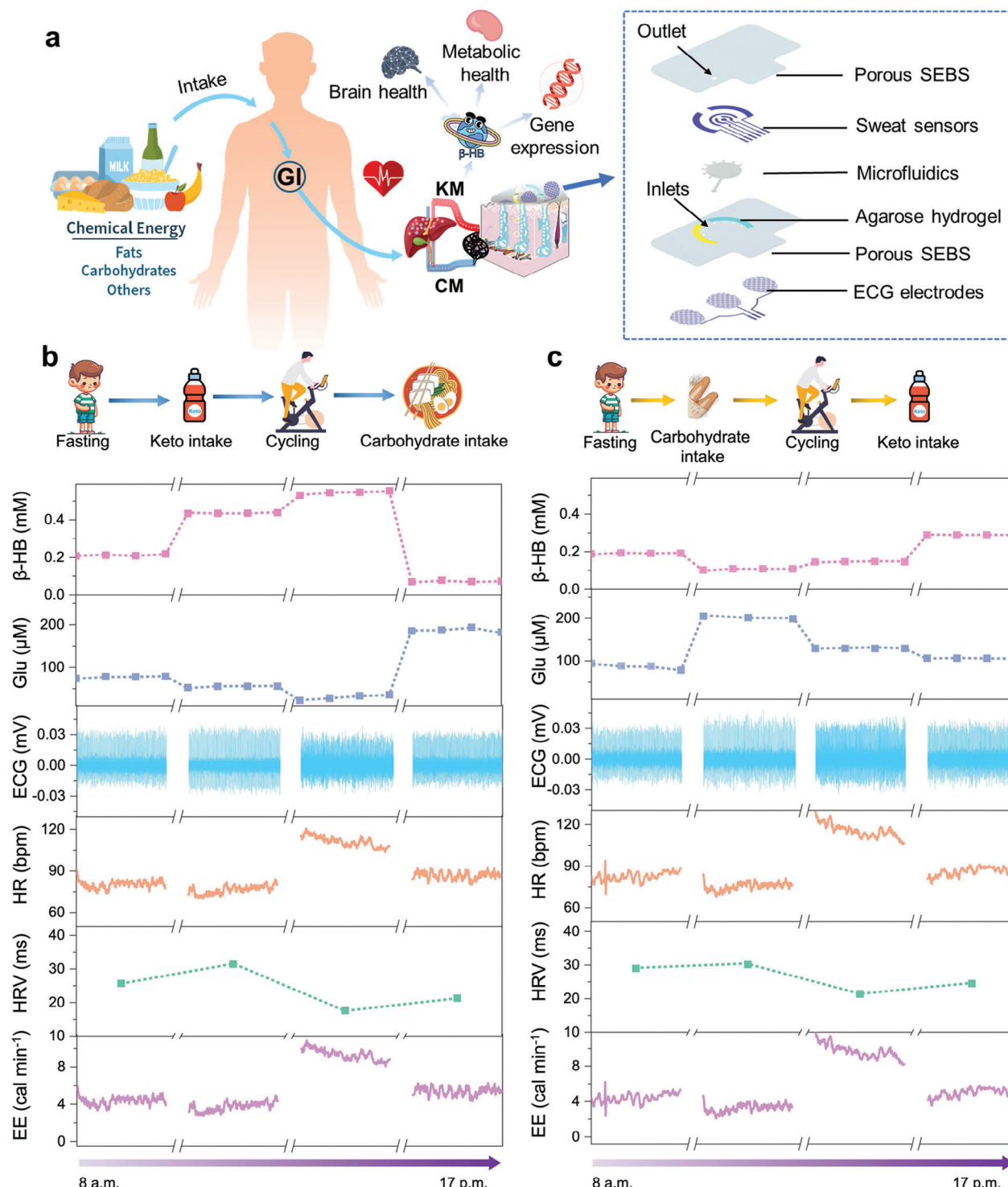


Figure 5. Porous wearable soft bioelectronics for energy metabolism and consumption monitoring. a) Conceptual illustration of human energy metabolism and consumption,^[41,42] which can be monitored by our multimodal porous soft bioelectronic devices. In brief, after food intake, the gastrointestinal (GI) system digests carbohydrates into glucose and fats into fatty acids and glycerol. These products are absorbed into the bloodstream and transported to cells. High blood glucose levels trigger carbohydrate metabolism (CM), while low glucose levels initiate the breakdown of fatty acids and glycerol, leading to ketone metabolism (KM) and the production of $\beta\text{-HB}$, essential for energy metabolism, brain health, and gene expression. Our multimodal porous soft bioelectronic devices can provide on-demand sweat extraction and real-time detections of glucose, $\beta\text{-HB}$, and ECG signals, which are closely related to energy metabolism and consumption. Concurrent monitoring of ECG and $\beta\text{-HB}$ and glucose levels from the upper arm of a human subject during the ketone-dominated (b) and carbohydrate-dominated (c) energy metabolic processes. Here, HR, HRV, and EE are determined from ECG signals.

metabolism-related biomarkers and ECG-derived energy consumption information makes it promising for offering valuable guidance to individuals seeking to manage their metabolic types and energy consumption.

3. Conclusion

By integrating CNF with porous substrates, our research marks substantial progress in enabling strain-resilient porous bioelectronics with high fidelity and advanced functions. Experimental results and theoretical simulations offer critical insights into the robust interface between CNF and porous substrates, highlight exceptional strain-resilient effects, and guide the design of microfluidic systems. Our prototype device indicates the potential of the reported technique to create advanced porous bioelectronic systems with customized multimodalities for precision human healthcare. Notably, the versatility of our technique extends beyond phase-separated porous substrates and PEDOT: PSS/AgNWs functional layers. It can also be applied to other porous soft substrates, such as fabrics and electrospun fibrous films (Figure S37, Supporting Information), as well as functional materials like carbon nanotubes (Figure S38, Supporting Information). This broad adaptability suggests a wide range of potential applications, paving the way for innovative solutions in precision healthcare and beyond. Moreover, the synergistic marriage of biomass-derived sustainable biomaterials with emerging bioelectronics highlights the eco-friendly benefits alongside technological advancements. Future work will focus on leveraging recent advancements in robot-enabled autonomous manufacturing systems^[50] to achieve scalable fabrication of CNF-enhanced multimodal porous soft bioelectronics with customized functionalities for diverse healthcare applications, such as heart monitoring, chronic wound management, and elderly care.

4. Experimental Section

Porous SEBS Synthesis: The porous SEBS was prepared using phase separation, following the previously published procedures.^[7] Briefly, 12 g of SEBS powder (H1062; Asahi Kasei) were dissolved in 200 mL of chloroform with continuous stirring. The resulting precursor solution was then mixed with isopropyl alcohol (IPA) in a 5:2 volume ratio. After thorough mixing via shaking and sonication, the mixed solution was drop-cast onto aluminum foils and allowed to dry at room temperature, resulting in the formation of porous SEBS films. Here, ϵ -polylysine modified with bis(2-ethylhexyl) sulfosuccinate (323 586, Sigma-Aldrich) was added (10% by weight) during phase separation to provide antibacterial properties.^{10[10,51]}

CNF Preparation: 10 g of softwood pulp (Lot No 0042, Nippon Paper Group, Japan) were thoroughly dispersed in 500 mL of distilled (DI) water under vigorous stirring. Subsequently, 0.16 g of TEMPO, 1 g of NaBr, and 30 mL of NaClO solution (12.5% by weight in water) were added sequentially into the dispersion to initiate the cellulose oxidation process. Throughout this procedure, the solution's pH was maintained at ≈ 10 by the addition of NaOH solutions, until the solution transitioned from yellow to colorless and maintained the stable pH. Following overnight stirring, the CNF was washed with DI water several times until the pH approached 7. The final CNF product was dried at 60 °C and stored for subsequent use.

Ink Preparation: For CNF extrusion-printing inks, prepared the inks of S-CNF, L-CNF, and mixed CNF. S-CNF inks were prepared by dispersing the previously obtained CNF into DI water at a specific ratio, followed by

sonication using a Branson SFX550 tip sonifier at 30% amplitude for 30 min. L-CNF inks were prepared by same procedures with S-CNF inks but using a low amplitude of 20%. For the mixed CNF inks, L-CNF inks was mixed with S-CNF inks with a ratio of 1:1.

The preparation of PEDOT: PSS inks for extrusion printing commenced with the freeze-drying of the PEDOT: PSS solution (Clevios PH1000, Heraeus Electronic Material) over a duration of 72 h, to yield PEDOT: PSS nanofibrils. Subsequently, these nanofibrils were re-dispersed in DI water to achieve a concentration of 10% by weight using a planetary mixer (AR-100, THINXY). The preparation of the composite inks of PEDOT: PSS and AgNWs for extrusion printing proceeded with the incorporation of 5% AgNWs ink (in DI water and ethylene glycol with a mass ratio of 3:2) into the 10% PEDOT: PSS inks with different ratios according to the applications. To adjust the final concentration of PEDOT: PSS to 5% by weight in the ink, additional ethylene glycol (EG), (3-glycidyloxypropyl) trimethoxysilane (GOPS, 440167-100ML, Sigma-Aldrich), and DI water were added. The solvent composition was finalized to water and EG with a mass ratio of 4:1, and the GOPS mass was adjusted to 5% of the PEDOT: PSS mass.

Ag NWs inks for inkjet printing were prepared by diluting the commercial Ag NWs (Ag NW-40, ACS Material) to a concentration of 0.2 mg mL⁻¹ in a mixed solution of isopropyl alcohol (IPA) and DI water at a 1:1 ratio, followed by sonication to reduce the lengths of the AgNWs to below 5 μ m. PEDOT: PSS inks for inkjet printing were prepared by adding 0.5% Triton X-100 into the commercial PEDOT: PSS solution (Clevios PH 1000) and mixed well in a bath sonication for 5 mins.

Extrusion printing and inkjet printing were performed on a specialized Microelectronic printer (Scientific 3, Mi Fang Electronics), adhering to a predefined patterning protocol. CNF inks underwent extrusion printing on plasma-treated, porous SEBS substrates following specific programmed patterns. Subsequently, conductive inks of PEDOT: PSS and AgNWs were printed atop designated CNF regions by either extrusion or inkjet printing in accordance with targeted applications to achieve high-quality printouts.

Fabrication of Biochemical Sensors and Iontophoresis Devices: The Na⁺ sensor comprises the reference and working electrodes, which were printed using composite inks of PEDOT: PSS and AgNWs. The reference electrode was coated with Ag/AgCl paste (CAT#011464, Allum Corp.), while the working electrode was coated with Na⁺ selective membranes (1 mg of Na ionophore, 0.55 mg of sodium tetrakis[3,5-bis(trifluoromethyl)phenyl] borate, 33 mg of polyvinyl chloride and 65.45 mg of Bis(2-ethylhexyl) sebacate in 660 μ L of tetrahydrofuran). Both the glucose and β -HB sensors comprises the reference, counter, and working electrodes, which were printed using composite inks of PEDOT: PSS and AgNWs. The reference electrode was coated with Ag/AgCl paste. The glucose working electrode was prepared by functionalizing the electrode with gold (Au) nanoparticles, Prussian blue (AC215210250, Fisher Scientific), and glucose oxidase (G7141, Sigma-Aldrich). The β -HB working electrode was prepared by functionalizing of the electrode with Au nanoparticles, toluidine blue O (TBO, Sigma-Aldrich), and β -hydroxybutyrate dehydrogenase (H9408, Sigma-Aldrich). The iontophoresis hydrogels were prepared by dissolving 0.6 g of agarose (A0169-50G, Sigma-Aldrich) in 20 mL of DI water using microwave heating (less than 1 min). The solution was then cooled to 165 °C, after which 6 mg of carbachol (10 222 275, Fisher Scientific) was added and thoroughly stirred. Next, the mixture was poured into a customized 3D-printed module and allowed to solidify at room temperature. For the preparation of cathode electrodes, carbachol was substituted with KCl. Agarose hydrogels loaded with carbachol on anodes and KCl on cathodes are employed for ionophoresis-enabled on-demand sweat extraction. Both of anodes and cathodes are made of printed PEDOT: PSS and AgNWs.

Fabrication of CNF-Based Microfluidics: The process started by dispersing prepared CNF in DI water with a concentration of 30 mg mL⁻¹ under vigorous stirring. This mixture was then transferred, measuring 10 mL, into a petri dish with a diameter of 90 mm and subsequently subjected to drying in an oven at 60 °C, facilitating the formation of an CNF membrane. Post-drying, the membrane underwent a hot-pressing procedure for 10 min, applying a pressure of 20 MPa and a temperature of 120 °C, to yield a densified membrane structure. The final membrane was then

precisely cut into the pre-designed shapes with a VLS2.30 universal laser system to obtain microfluidic systems.

Device Fabrication and Integration with Flexible Circuits: The multimodal porous patch in Figure 5a was created through a series of fabrication steps. First, CNF interfaces were printed onto porous SEBS. Next, the electrodes for ECG monitoring and biochemical sensing were inkjet-printed onto designated layers. A VLS2.30 universal laser system was employed to cut designed patterns, creating inlets, outlets, and designated areas for iontophoresis devices. Upon completing these individual components, the layers with ECG sensors, microfluidic systems, and biochemical sensors were assembled from bottom to top using breathable double-sided adhesive tapes (3M Medical Tape 9917). The flexible printed circuit board was subsequently connected to the multimodal porous patch using flexible flat cables (Premo-Flex, Molex) and Z-axis conductive tapes (Adafruit). To enhance the device's adhesion and ensure conformal contact with the skin, the porous SEBS on the skin-facing side was coated with water-based acrylic pressure-sensitive adhesives.^[52]

Characterization and Measurement: SEM images were taken using FEI Quanta 600F Environmental SEM Helios Hydra UX DualBeam SEM. Transmission electron microscopy (TEM) images were collected with JEOL JEM-1400 TEM. Surface roughness was measured using an optical profilometer (Veco NT 9109). 3D Digital Image Correlation System Q-400 (Dantec Dynamics, Tonsbakken, Skovlunde, Denmark) was utilized for measurements of strain distribution during stretching. ECG measurements were validated and conducted using PowerLab T26 (AD Instruments). Electrochemical characterizations were conducted using an electrochemical station (CHI660E, CH Instruments Inc.). The electrical and mechanical tests were conducted with a dual-channel source meter (2604B, Keithley Instruments) and Mark-10 ESM303 tensile tester. For on-body monitoring of energy metabolism and consumption, the porous wearable bioelectronic device was adhered to the upper arm of a human volunteer. The iontophoresis was initiated for 5 min to stimulate sweat production. Following this, physiological data and sweat biochemical data were continuously collected for 2 min under each specified condition.

Antibacterial Activity: The investigation into the materials' antibacterial properties was conducted against three types of bacterial strains, including *Staphylococcus aureus* (MRSA), *Escherichia coli* (EC), and *Pseudomonas aeruginosa* (PA), following previously reported procedures.^[10] In brief, the samples were separately added to 1 mL of respective bacterial suspension (10^8 CFU mL⁻¹) in PBS and incubated at 37 °C for 6 h. At the set time point, following the dilution of a bacterial solution by a factor of 1000, 10 µL of the solution was spread onto the LB-agar plate and the log reduction of bacteria was calculated. Additionally, a live-dead assay was conducted to assess viability of bacteria. This was achieved using the LIVE/DEAD Bacterial Viability Kit from Invitrogen.

Cytocompatibility and Hemocompatibility Assay: The materials' cytotoxicity was assessed in four types of cell lines, keratinocytes (HaCaT), monocytes (U937), neutrophils (HL-60), and human dermal fibroblasts (HDF- α), using previously reported procedures.^[10] Briefly, for HaCaT, and HDF- α , the DMEM media supplemented with 10% FBS and 1% penicillin-streptomycin was used to culture, while an RPMI 1640 media supplemented with 10% FBS and 1% penicillin-streptomycin was used to grow U937 and HL-60. The cells were seeded in a 48-well plate at a density of 10^4 cells/well, and the sterilized and pre-cut (1 × 1 cm) samples were transferred to each well using well-inserts. The cells were incubated at 37 °C for 3 days, and cell toxicity was determined by adding 20 µL of Cell Counting Kit-8 (CCK-8) per well, and absorbance was measured at 450 nm using a microplate reader. In addition, following staining using the LIVE/DEAD cell viability kit (Thermo Fisher Scientific, USA), the cells were examined using an inverted fluorescence microscope (Zeiss, Germany).

Hemolysis Test: The hemolysis assay was performed to examine the materials' blood compatibility using previously reported procedures.^[53] In brief, the anticoagulated human blood was centrifuged at 1500 rpm for 10 min, and the pellet of Red blood cells (RBCs) that had been obtained was washed with PBS. Subsequently, the RBCs were diluted to achieve a final RBC concentration of 10.0% (by volume). 200 µL of the solution was added to each sample and kept for 1 h at 37 °C. Later, the samples were collected after centrifugation and absorbance was measured at 540 nm.

Additionally, the positive control (100%) was generated using 1% Triton-X, while the negative control (0%) was prepared without any treatment.

Numerical Simulations of Strain Engineering: FEA simulations for strain engineering were conducted with COMSOL Multiphysics version 6.0. Within these simulations, the "Stationary Study" feature was engaged through the "Solid Mechanics Interface." A hyperelastic, incompressible Mooney-Rivlin model, characterized by five parameters, was employed for the analysis. The prescribed displacements were applied on the gripped region and the strain and stress field were calculated in regions near CNF interfaces.

Numerical Simulations of Sweat Dynamics in Microfluidics: All fluidic simulations in Figure 4, Figures S28 and S29 (Supporting Information) were performed with COMSOL Multiphysics version 6.0. To simulate the process of sweat filling in an empty CNF channel, a computational fluid dynamics module (Two-Phase Flow, Level Set interface) was used. Additionally, the solute diffusion was modeled using a combination of the "Transport of Diluted Species Interface" and the "Laminar Flow Interface". The concentration of the solute at the center of the circular channel was monitored over time to determine the refresh time.

Molecular Dynamics Simulations: Molecular dynamic simulations were conducted using LAMMPS. The Polymer-Consistent Force Field was used to model the interaction parameters for the polymer systems. The pristine molecular configurations were performed under the canonical (NVT) ensemble in a vacuum at a constant temperature of 300 K during the simulation time of 500 ps. The Nosé–Hoover style barostat and thermostat were used to control the pressure and temperature. The energy-minimized and dynamically optimized SEBS/cellulose system was run under NVT conditions for 2000 ps to investigate hydrogen bonding interactions and structural information.

Experiments on Human Participants: All experiments were conducted under approval from the Institutional Review Board at the University of Missouri at Columbia (#2 010 272). All human subjects gave written and informed consent before participation in the studies.

Statistical Analysis: The statistical analysis was performed using GraphPad Prism 8.0 software. Differences among groups were evaluated using one-way analysis of variance (ANOVA) followed by Tukey's multiple comparisons test. The values of $p < 0.05$ were considered statistically significant.

Supporting Information

Supporting Information is available from the Wiley Online Library or from the author.

Acknowledgements

G.Z. and Z.C. contributed equally to this work. Z.Y. acknowledges the financial support from the start-up fund of the University of Missouri at Columbia. Z.Y. and J.X. acknowledge the financial support from the National Institute of Biomedical Imaging and Bioengineering (R01EB033371). The human study was supported by Z.Y.'s start-up fund. The authors acknowledge Lin Shi and Matthew Sabirianov for the technical assistance.

Conflict of Interest

The authors declare no conflict of interest.

Data Availability Statement

The data that support the findings of this study are available from the corresponding author upon reasonable request.

Keywords

metabolism and consumption monitoring, microfluidics, nanofibril interfaces, porous soft bioelectronics, strain resilience

Received: August 6, 2024
Revised: September 17, 2024

Published online:

- [1] T. Someya, M. Amagai, *Nat. Biotechnol.* **2019**, *37*, 382.
- [2] S. Liu, Y. Rao, H. Jang, P. Tan, N. Lu, *Matter* **2022**, *5*, 1104.
- [3] J. Yin, S. Wang, T. Tat, J. Chen, *Nat. Rev. Bioeng.* **2024**, *2*, 541.
- [4] A. Miyamoto, S. Lee, N. F. Cooray, S. Lee, M. Mori, N. Matsuhisa, H. Jin, L. Yoda, T. Yokota, A. Itoh, M. Sekino, H. Kawasaki, T. Ebihara, M. Amagai, T. Someya, *Nat. Nanotechnol.* **2017**, *12*, 907.
- [5] B. Zhang, J. Li, J. Zhou, L. Chow, G. Zhao, Y. Huang, Z. Ma, Q. Zhang, Y. Yang, C. K. Yiu, J. Li, F. Chun, X. Huang, Y. Gao, P. Wu, S. Jia, H. Li, D. Li, Y. Liu, K. Yao, R. Shi, Z. Chen, B. L. Kho, W. Yang, F. Wang, Z. Zheng, Z. Wang, X. Yu, *Nature* **2024**, *628*, 84.
- [6] Z. Ma, Q. Huang, Q. Xu, Q. Zhuang, X. Zhao, Y. Yang, H. Qiu, Z. Yang, C. Wang, Y. Chai, Z. Zheng, *Nat. Mater.* **2021**, *20*, 859.
- [7] Y. Xu, B. Sun, Y. Ling, Q. Fei, Z. Chen, X. Li, P. Guo, N. Jeon, S. Goswami, Y. Liao, S. Ding, Q. Yu, J. Lin, G. Huang, Z. Yan, *Proc. Natl. Acad. Sci. USA* **2020**, *117*, 205.
- [8] J. Mandal, Y. Fu, A. C. Overvig, M. Jia, K. Sun, N. N. Shi, H. Zhou, X. Xiao, N. Yu, Y. Yang, *Science* **2018**, *362*, 315.
- [9] P. C. Hsu, A. Y. Song, P. B. Catrysse, C. Liu, Y. Peng, J. Xie, S. Fan, Y. Cui, *Science* **2016**, *353*, 1019.
- [10] Y. Xu, Y. Su, X. Xu, B. Arends, G. Zhao, D. N. Ackerman, H. Huang, S. P. Reid, J. L. Santarpia, C. Kim, Z. Chen, S. Mahmoud, Y. Ling, A. Brown, Q. Chen, G. Huang, J. Xie, Z. Yan, *Sci. Adv.* **2023**, *9*, eadf0575.
- [11] S. Zheng, W. Li, Y. Ren, Z. Liu, X. Zou, Y. Hu, J. Guo, Z. Sun, F. Yan, *Adv. Mater.* **2022**, *34*, 2106570.
- [12] K. I. Jang, S. Y. Han, S. Xu, K. E. Mathewson, Y. Zhang, J. W. Jeong, G. T. Kim, R. C. Webb, J. W. Lee, T. J. Dawidczyk, R. H. Kim, Y. M. Song, W. H. Yeo, S. Kim, H. Cheng, S. I. Rhee, J. Chung, B. Kim, H. U. Chung, D. Lee, Y. Yang, M. Cho, J. G. Gaspar, R. Carbonari, M. Fabiani, G. Gratton, Y. Huang, J. A. Rogers, *Nat. Commun.* **2014**, *5*, 4779.
- [13] Y. Xu, Z. Ye, G. Zhao, Q. Fei, Z. Chen, J. Li, M. Yang, Y. Ren, B. Berigan, Y. Ling, X. Qian, L. Shi, I. Ozden, J. Xie, W. Gao, P. Y. Chen, Z. Yan, *Nat. Nanotechnol.* **2024**, *19*, 1158.
- [14] B. Sun, R. N. McCay, S. Goswami, Y. Xu, C. Zhang, Y. Ling, J. Lin, Z. Yan, *Adv. Mater.* **2018**, *30*, 1804327.
- [15] Y. Wang, T. Yokota, T. Someya, *NPG Asia Mater* **2021**, *13*, 22.
- [16] P. Wang, X. Ma, Z. Lin, F. Chen, Z. Chen, H. Hu, H. Xu, X. Zhang, Y. Shi, Q. Huang, Y. Lin, Z. Zheng, *Nat. Commun.* **2024**, *15*, 887.
- [17] G. Zhao, Y. Ling, Y. Su, Z. Chen, C. J. Mathai, O. Emeje, A. Brown, D. R. Alla, J. Huang, C. Kim, *Sci. Adv.* **2022**, *8*, eabp9734.
- [18] Q. Zhuang, K. Yao, M. Wu, Z. Lei, F. Chen, J. Li, Q. Mei, Y. Zhou, Q. Huang, X. Zhao, Y. Li, X. Yu, Z. Zheng, *Sci. Adv.* **2023**, *9*, eadg8602.
- [19] T. Zhou, H. Yuk, F. Hu, J. Wu, F. Tian, H. Roh, Z. Shen, G. Gu, J. Xu, B. Lu, X. Zhao, *Nat. Mater.* **2023**, *22*, 895.
- [20] Y. Song, R. Y. Tay, J. Li, C. Xu, J. Min, E. Shirzaei Sani, G. Kim, W. Heng, I. Kim, W. Gao, *Sci. Adv.* **2023**, *9*, eadi6492.
- [21] Y. Yu, J. Li, S. A. Solomon, J. Min, J. Tu, W. Guo, C. Xu, Y. Song, W. Gao, *Sci. Robot.* **2022**, *7*, eabn0495.
- [22] T. Li, C. Chen, A. H. Brozena, J. Y. Zhu, L. Xu, C. Driemeier, J. Dai, O. J. Rojas, A. Isogai, L. Wagberg, L. Hu, *Nature* **2021**, *590*, 47.
- [23] Y. Xu, Q. Fei, M. Page, G. Zhao, Y. Ling, S. B. Stoll, Z. Yan, *iScience* **2021**, *24*, 102736.
- [24] H. Tu, M. Zhu, B. Duan, L. Zhang, *Adv. Mater.* **2021**, *33*, 2000682.
- [25] X. Shi, Z. Wang, S. Liu, Q. Xia, Y. Liu, W. Chen, H. Yu, K. Zhang, *Nat. Sustain.* **2024**, *7*, 315.
- [26] X. Yang, K. Abe, S. K. Biswas, H. Yano, *Cellulose* **2018**, *25*, 6571.
- [27] W. Cheng, Y. Zhu, G. Jiang, K. Cao, S. Zeng, W. Chen, D. Zhao, H. Yu, *Prog. Mater. Sci.* **2023**, *138*, 101152.
- [28] D. Roy, M. Semsarilar, J. T. Guthrie, S. Perrier, *Chem. Soc. Rev.* **2009**, *38*, 2046.
- [29] E. Abraham, V. Cherpak, B. Senyuk, J. B. ten Hove, T. Lee, Q. Liu, I. I. Smalyukh, *Nat. Energy* **2023**, *8*, 381.
- [30] J. Lessing, A. C. Glavan, S. B. Walker, C. Keplinger, J. A. Lewis, G. M. Whitesides, *Adv. Mater.* **2014**, *26*, 4677.
- [31] M. Kuang, L. Wang, Y. Song, *Adv. Mater.* **2014**, *26*, 6950.
- [32] S. Chao, Y. Li, R. Zhao, L. Zhang, Y. Li, C. Wang, X. Li, *J. Drug Deliv. Sci. Technol.* **2018**, *44*, 440.
- [33] M. Namkoong, H. Guo, M. S. Rahman, D. Wang, C. J. Pfeil, S. Hager, L. Tian, *npj Flex. Electron.* **2022**, *6*, 41.
- [34] N. Gao, J. Yu, Q. Tian, J. Shi, M. Zhang, S. Chen, L. Zang, *Chemosensors* **2021**, *9*, 79.
- [35] S. Liu, D. S. Shah, R. Kramer-Bottiglio, *Nat. Mater.* **2021**, *20*, 851.
- [36] Y. Yang, Y. Song, X. Bo, J. Min, O. S. Pak, L. Zhu, M. Wang, J. Tu, A. Kogan, H. Zhang, T. K. Hsiai, Z. Li, W. Gao, *Nat. Biotechnol.* **2020**, *38*, 217.
- [37] C. Xu, Y. Song, J. R. Sempionatto, S. A. Solomon, Y. Yu, H. Y. Y. Nyein, R. Y. Tay, J. Li, W. Heng, J. Min, A. Lao, T. K. Hsiai, J. A. Sumner, W. Gao, *Nat. Electro.* **2024**, *7*, 168.
- [38] C. Ye, M. Wang, J. Min, R. Y. Tay, H. Lukas, J. R. Sempionatto, J. Li, C. Xu, W. Gao, *Nat. Nanotechnol.* **2023**, *19*, 330.
- [39] J. Tu, J. Min, Y. Song, C. Xu, J. Li, J. Moore, J. Hanson, E. Hu, T. Parimon, T. Y. Wang, E. Davoodi, T. F. Chou, P. Chen, J. J. Hsu, H. B. Rossiter, W. Gao, *Nat. Biomed. Eng.* **2023**, *7*, 1293.
- [40] M. Liu, J. Wu, Y. Gan, D. A. H. Hanaor, C. Q. Chen, *Langmuir* **2016**, *32*, 9899.
- [41] R. de Cabo, M. P. Mattson, *N. Engl. J. Med.* **2019**, *381*, 2541.
- [42] Y. He, X. Cheng, T. Zhou, D. Li, J. Peng, Y. Xu, W. Huang, *Heliyon* **2023**, *9*, e21098.
- [43] F. Shaffer, J. P. Ginsberg, *Front. Public Health* **2017**, *5*, 258.
- [44] L. Keytel, J. Goedcke, T. D. Noakes, H. Hiiloskorpi, R. Laukkonen, L. van der Merwe, E. Lambert, *J. Sports Sci.* **2005**, *23*, 289.
- [45] N. Uth, H. Sorensen, K. Overgaard, P. K. Pedersen, *Eur. J. Appl. Physiol.* **2004**, *91*, 111.
- [46] N. A. Taylor, C. A. Machado-Moreira, *Extrem. Physiol. Med.* **2013**, *2*, 4.
- [47] C. J. Smith, G. Havenith, *Eur. J. Appl. Physiol.* **2011**, *111*, 1391.
- [48] J.-J. Wang, S.-H. Liu, C.-H. Tsai, I. Manousakis, X. Zhu, T.-L. Lee, *Sensors* **2023**, *23*, 5818.
- [49] Y. Khan, M. L. Mauriello, P. Nowruzi, A. Motani, G. Hon, N. Vitale, J. Li, J. Kim, A. Foudeh, D. Duvio, *bioRxiv* **2021**, *2021.01.20.427496*.
- [50] B. Zheng, Y. Xie, S. Xu, A. C. Meng, S. Wang, Y. Wu, S. C. Wan, G. Huang, J. M. Tour, J. Lin, *Nat. Commun.* **2024**, *15*, 454.
- [51] K. Ushimaru, Y. Hamano, H. Katano, *Biomacromolecules* **2017**, *18*, 1387.
- [52] D. McManus, S. Vranic, F. Withers, V. Sanchez-Romaguera, M. Macucci, H. Yang, R. Sorrentino, K. Parvez, S. K. Son, G. Iannaccone, K. Kostarelos, G. Fiori, C. Casiraghi, *Nat. Nanotechnol.* **2017**, *12*, 343.
- [53] P. Singh, S. M. Andrabi, U. Tariq, S. Gupta, S. Shaikh, A. Kumar, *J. Chem. Engin.* **2023**, *457*, 141359.